Chem Soc Rev

Chemical Society Reviews

www.rsc.org/chemsocrev

Volume 37 | Number 4 | April 2008 | Pages 613–872

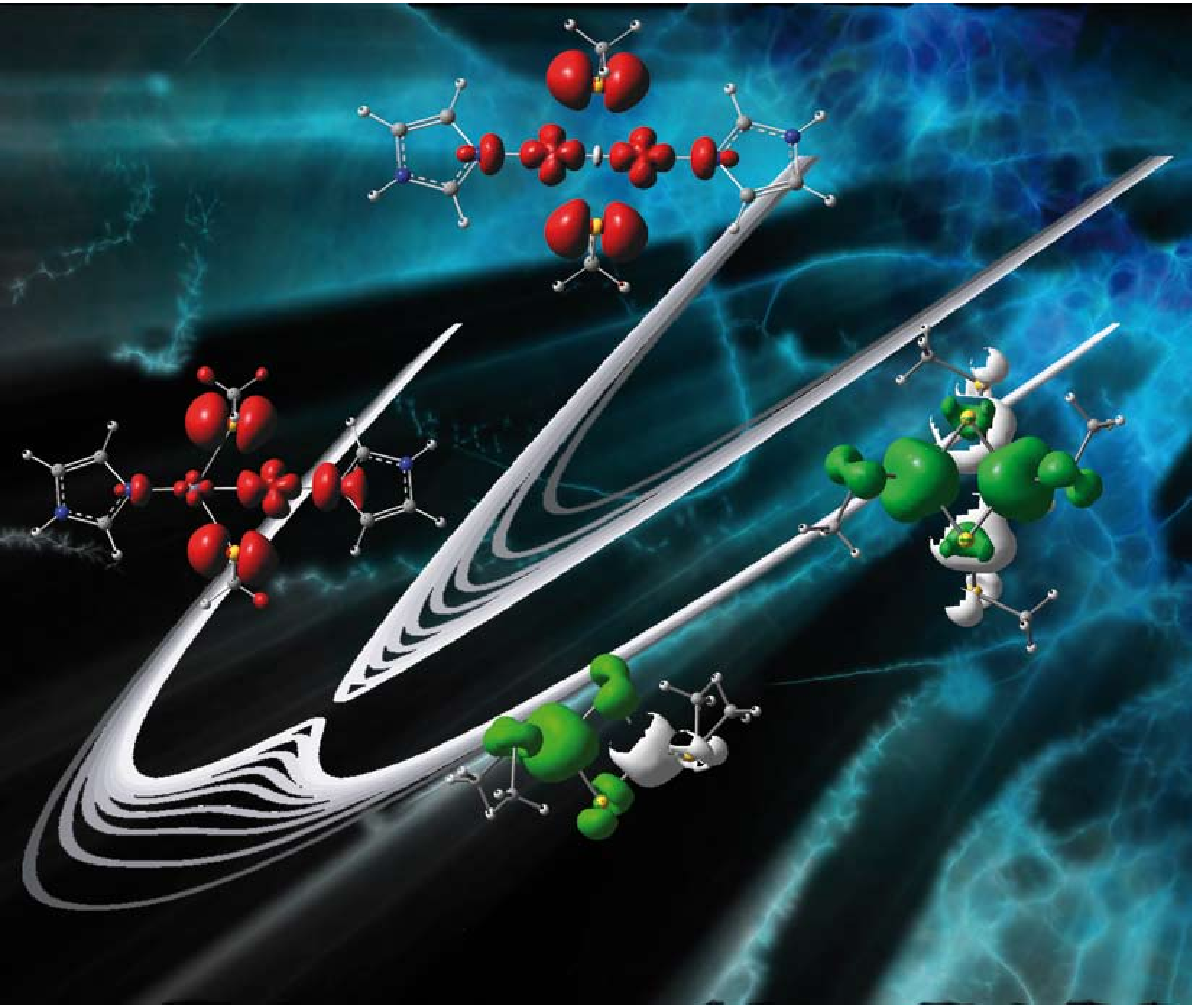

ISSN 0306-0012

RSC Publishing

TUTORIAL REVIEW
Edward I. Solomon, Xiangjin Xie and Abhishek Dey
Mixed valent sites in biological electron transfer

THEMATIC ISSUE
A critical review and five tutorial reviews on the theme of gas kinetics are included in this issue

0306-0012(2008)37:4;1-9

Mixed valent sites in biological electron transfer

Edward I. Solomon,* Xiangjin Xie and Abhishek Dey

Received 5th January 2008
First published as an Advance Article on the web 11th February 2008
DOI: 10.1039/b714577m

Many of the active sites involved in electron transfer (ET) in biology have more than one metal and are mixed valent in at least one redox state. These include Cu_A, and the polynuclear Fe–S clusters which vary in their extent of delocalization. In this *tutorial review* the relative contributions to delocalization are evaluated using S K-edge X-ray absorption, magnetic circular dichroism and other spectroscopic methods. The role of intra-site delocalization in ET is considered.

Introduction

Fig. 1 summarizes the metal sites presently known to be involved in biological electron transfer (ET).[1–3] In Cu bioinorganic chemistry, these are the blue copper and Cu_A sites. Both have Cu centers in trigonal ligand fields. Blue copper sites have a highly covalent thiolate and two histidine (His) equatorial ligands, and a weak axial ligand, while each metal center in Cu_A has a His and two bridging thiolate equatorial ligands with additional weak *trans* axial ligands, one on each copper.[4,5] Rubredoxins, ferredoxins (Fds) and high potential iron–sulfur proteins (HiPIPs) have 1 to 4 Fe atoms in distorted tetrahedral fields of bridging sulfide and terminal thiolate ligands. The Fe centers are high-spin in all redox states. The cytochromes have heme Fe sites with two additional axial ligands creating a strong ligand field and low-spin Fe centers. In all cases, the ligand field and protein environment tune the reduction potential of the sites into their physiological range,[3] and ET is rapid with a low reorganization energy (λ, little change in geometry with redox) and large electronic coupling through the protein (H_{DA}) activating electron transfer.[6,7]

Department of Chemistry, Stanford University, Stanford, California 94305, USA. E-mail: edward.solomon@stanford.edu

In past reviews, our focus has been on the blue copper site and how its unique spectroscopic properties reflect a novel electronic structure activated for rapid ET.[8,9] Here, we consider the binuclear and higher nuclearity clusters, and how their mixed valent (MV) properties reflect electronic structures tuned for ET. In Cu_A, a Cu–Cu bonding interaction at 2.4 Å keeps the MV oxidized site delocalized even in its low symmetry protein environment. In the iron sulfur clusters, the reduced $[Fe_2S_2]^{1+}$ site is localized and antiferromagnetically (AF) coupled, while the $[Fe_2S_2]^{1+}$ subsite of the Fe_3S_4 and Fe_4S_4 clusters is delocalized and ferromagnetically coupled. Finally we will evaluate how the protein tunes the redox properties of these metal cluster sites in biology.

The Cu_A site

The reduced Cu_A center has $[2Cu]^{2+}$ which are oxidized by one electron to a MV $[2Cu]^{3+}$ center. In the oxidized binuclear Cu center, the extra electron can be either localized on Cu_a (with a wavefunction given by $\psi[Cu_a(\text{I})Cu_b(\text{II})]$), localized on Cu_b (wavefunction = $\psi[Cu_a(\text{II})Cu_b(\text{I})]$), or delocalized between the two Cu centers as described by eqn (1).[10]

Edward I. Solomon received his PhD from Princeton University and was a Postdoctoral Fellow at the Ørsted Institute of the University of Copenhagen and at Caltech. He was a Professor at MIT and is now the Monroe E. Spaght Professor of Humanities and Sciences at Stanford University. His research is in the fields of physical-inorganic and bioinorganic chemistry with emphasis on the application of a wide variety of spectroscopic and computational methods to elucidate the electronic structures of transition metal complexes and their contributions to physical properties and reactivity.

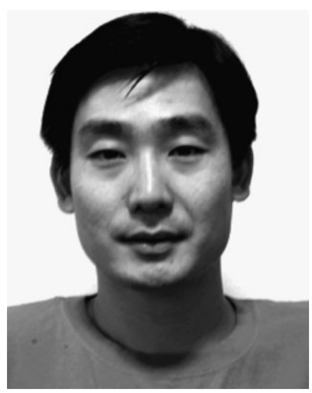

Xiangjin Xie received his BS degree in Chemistry from Peking University, Beijing, and then graduated with an MS degree from the same university under the guidance of Prof. Kaluo Tang and Prof. Xianglin Jin. He is currently working toward his PhD in chemistry at Stanford University under the direction of Prof. Edward I. Solomon. His research interests focus on bioinorganic spectroscopy, in particular on electron transfer proteins.

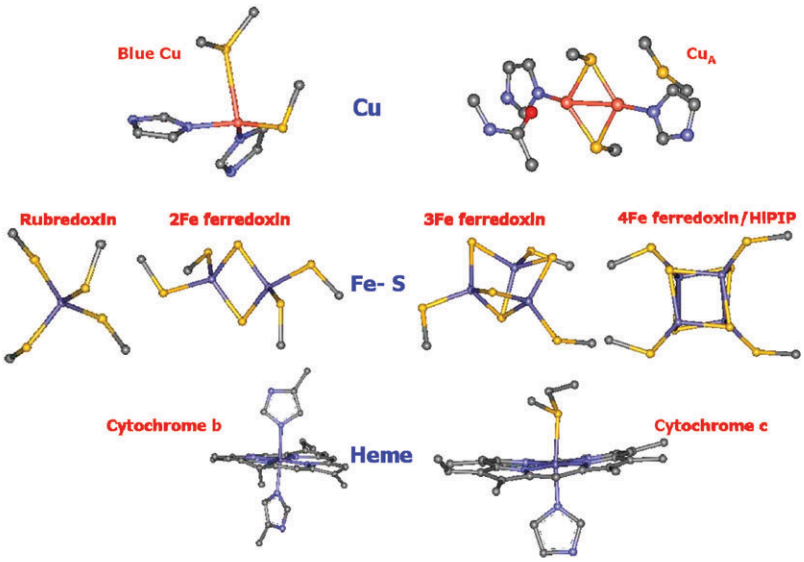

Fig. 1 Electron transfer sites in bioinorganic chemistry.

$$\psi_{\mathrm{ground}} = (1 - \alpha^2)^{1/2}\psi[\mathrm{Cu_a(I)Cu_b(II)}] + \alpha\psi[\mathrm{Cu_a(II)Cu_b(I)}] \quad (1)$$

In the Robin and Day classification scheme,[11] MV complexes are characterized as class I, II or III based on the value of α^2, the extent of delocalization. A site with the extra electron completely localized, $\alpha^2 = 0$, is called a class I MV complex. In class II MV sites, partial delocalization of the extra electron occurs (*i.e.* $0 < \alpha^2 < 0.5$). The completely delocalized case ($\alpha^2 = 0.5$) corresponds to the class III MV limit, which exhibits strikingly different spectroscopic features from those of the individual localized cases. For Cu$_A$, its electron paramagnetic resonance (EPR) signal (*vide infra*) exhibits equal hyperfine couplings of the unpaired electron to both Cu centers.[12] This indicates that Cu$_A$ is at the delocalized Class III limit. The extent of delocalization is determined by the electronic coupling, H_{AB}, associated with bonding interactions between the valence orbitals on Cu$_a$ and Cu$_b$. Note that this electronic coupling can involve both direct exchange of the valence orbitals of the two metals and superexchange through the bridging ligands.

An oxidized metal center will generally have shorter metal–ligand bond lengths than a reduced metal center. This distortion (symmetric contraction or elongation of all ligand–metal bonds of metal centers A and B in their breathing modes, Q_A and Q_B) in an MV site gives an energy stabilization term that can trap the oxidation on the ligand contracted metal center. This is shown in Chart 1. Following the Piepho, Krausz and Schatz (PKS) model in the Q_- mode, which is the antisymmetric combination of the breathing modes ($Q = 2^{-1/2}(Q_A - Q_B)$, bottom of Chart 1),[13] the combined effect of electronic coupling, H_{AB}, and vibronic trapping, $\frac{1}{\sqrt{2}}\lambda Q_-$, on the delocalization of the ground state is given by eqn (2) in terms of the dimensionless coordinate $x\_$ ($x\_ = (k\_/\lambda)Q\_$, $k\_$ is force constant and λ is the vibronic coupling parameter where $\lambda \approx k\_(n^{1/2}\Delta r_{\mathrm{redox}})$, in which n is the number of metal–ligand bonds and $\Delta r_{\mathrm{redox}}$ is the difference in the metal–ligand bond length between the oxidized and reduced centers). The fact that the Cu$_A$ center is a class III MV system indicates that the electronic coupling has overcome the vibronic trapping for this site. This lack of vibronic trapping plays a significant role in lowering the Frank-Condon

Abhishek Dey obtained his BSc from Presidency College, Calcutta, and an MSc degree in Chemistry from the Indian Institute of Technology, Kanpur. He obtained his PhD at Stanford University with Prof. Edward I. Solomon, Prof. Britt Hedman and Prof. Keith O. Hodgson. He is currently a post-doctoral research associate of Prof. J. P. Collman at the Department of Chemistry, Stanford University.

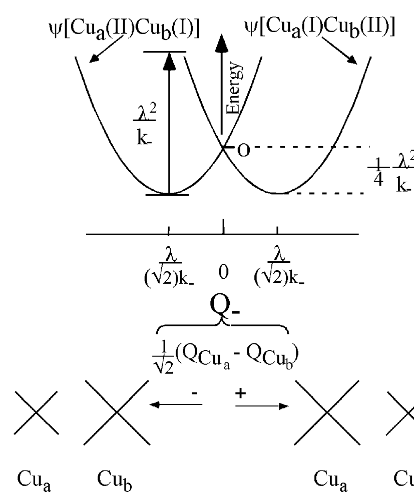

Chart 1

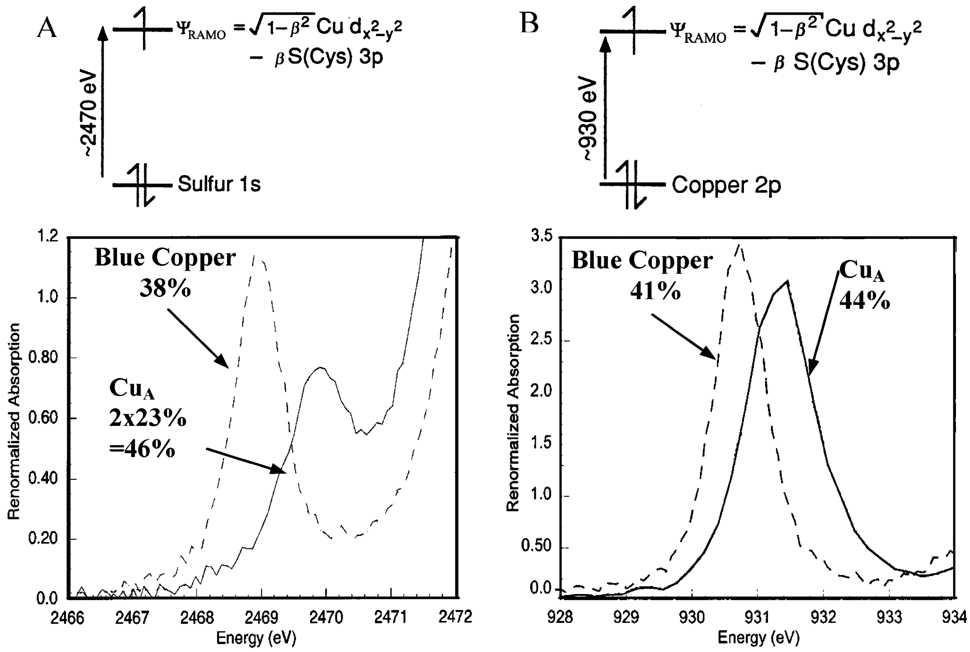

Fig. 2 S K-edge and Cu L-edge XAS as probes of ligand-to-metal covalency. (a) Comparison of S K-edge spectra of blue copper and Cu_A (bottom), energy level diagram depicting S 1s to RAMO transition (top), β^2 is the amount of S p character in the RAMO. (b) Comparison of Cu L-edge spectra of blue copper and Cu_A (bottom), energy level diagram depicting Cu 2p to RAMO transition (top).

barrier to ET by the Cu_A center in biology (*vide infra*).

$$E^{\pm} = \frac{1}{2}\left(\frac{\lambda^2}{k_-}\right)x_-^2 \pm \left[\frac{1}{2}\left(\frac{\lambda^2}{k_-}\right)^2 x_-^2 + H_{AB}^2\right]^{1/2} \qquad (2)$$

We first consider how the covalency of this center correlates to that of the very well documented[8,9] blue copper site. Ligand K-edge and metal L-edge X-ray absorption spectroscopies (XAS) provide direct probes of the ligand and metal character in their 1/2 occupied, redox active molecular orbital (RAMO). The S pre-edge at 2470 eV reflects the transition from the S 1s orbital to the RAMO. Since the 1s orbital is localized on the sulfur and s → p is electron dipole allowed, the intensity of the S pre-edge is directly proportional to the S 3p character mixed into the RAMO due to covalent interaction with the metal, *i.e.*, the covalency of the sulfur–metal bond. From Fig. 2A, the intensity of the blue copper pre-edge is about twice that of Cu_A. However, for Cu_A, the pre-edge reflects the covalency/thiolate and must be doubled; therefore Cu_A has about the same thiolate character as blue copper, but delocalized over the two thiolates (38% S 3p in blue Copper, 46% S 3p in Cu_A).[14] We will continue to use this S K-edge XAS method throughout this review to define the covalency of active sites.

The Cu L pre-edge at 930 eV reflects the Cu 2p → RAMO transition (Fig. 2B top). The 2p orbital is localized on the Cu nucleus and p → d is electronic-dipole-allowed; therefore, the intensity of these pre-edges also reflects covalency, in this case the Cu d character in the RAMO. From Fig. 2B, blue copper and Cu_A both have about the same Cu L-edge integrated intensity, therefore Cu d characters in their RAMO's (41% Cu d in blue copper, 44% Cu d in Cu_A), however again for Cu_A, this is delocalized over the two Cu centers.

The highly-covalent delocalized ground state wavefunction of Cu_A makes major contributions to rapid ET.[14] From Fig. 3, the high covalency of the sulfur bridges activates specific superexchange pathways for ET. Cu_A is found in cytochrome *c* oxidase (and N_2O reductase) and functions to take an electron from cytochrome *c* and transfer it rapidly to heme *a*; this involves long distances (> 18 Å) with a low driving force. Fig. 3 shows that the high thiolate covalency activates pathways for ET into the buried Cu_A center and from Cu_A to heme *a*. For the ET to heme *a*, there are multiple pathways allowing for possible constructive and destructive interference. Further, the delocalized nature of Cu_A distributes the geometry change associated with redox over twice the number of bonds as in a localized site, but with half of the distortion in each bond. As the reorganization energy (λ_{reorg}) in Marcus theory[6] goes as the distortion squared ($\lambda_{reorg} \approx k_{dis}n(\Delta r)^2$, this decreases the reorganization energy by 1/2 and leads to a 15-fold increase in k_{ET}.[15]

Also from the pre-edge energies in Fig. 2, the RAMO of Cu_A is 0.8 eV higher in energy than that of blue copper even though these have similar trigonal ligand fields. This must then reflect a bonding interaction between the Cu's at R_{Cu-Cu} = 2.4 Å. This has been probed directly by absorption (Abs) and resonance Raman (rR) spectroscopies.[16,17]

Fig. 4C shows the Abs spectrum of Cu_A. There are two regions: the bands at ~20 000 cm^{-1} are thiolate to Cu charge transfer (CT) transitions as indicated by rR into these bands which shows enhancement in the symmetric, in-phase breathing mode at 337 cm^{-1}(ν_4), and in the Cu–S and Cu–N bond distortions at 260 cm^{-1} (ν_2) and 270 cm^{-1} (ν_3) (Fig. 4B solid line). Alternatively, excitation into the Abs band at 13 400 cm^{-1} produces the rR spectrum given by the dashed line in Fig. 4B which shows only distortions in the breathing mode

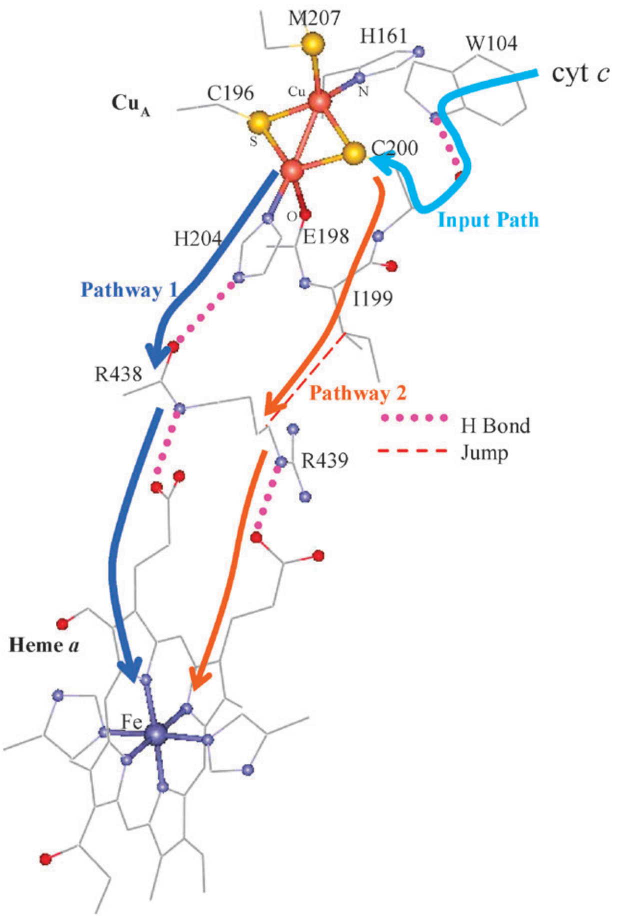

Fig. 3 Proposed ET pathways in bovine heart CcO based on Pathways analysis. The Cys200 and His204 Cu$_A$-to-heme *a* pathways are comparable in rate.

(ν_4) and the symmetric out-of-phase accordion mode (ν_1) indicating a change in the Cu–Cu distance.[16–18] From the rR intensities, the exited state distortion associated with this electronic transition can be estimated as a 0.44 Å elongation in the Cu–Cu bond with no change in Cu–L bond lengths.[19] This transition is assigned as the Cu–Cu $\psi \rightarrow \psi^*$ transition (a transition between the Cu–Cu bonding-to-antibonding molecular orbitals of the class III MV system) with distortions only along the symmetric vibrational modes of the Cu_2S_2 core, consistent with the completely delocalized nature of the ground state associated with a strong Cu–Cu interaction at 2.4 Å.

The bonding contributions to the Cu–Cu interaction in Cu$_A$ were elucidated by comparison to a class III MV model complex (Chart 2A) reported by Tolman and coworkers.[16,20,21] This complex has a Cu–Cu bond length of 2.9 Å, which eliminates the direct Cu–Cu bonding contribution to the interaction between the Cu's leading to delocalization. By comparison of the low temperature Abs/MCD spectra in Fig. 5 of the MV complex in red to the spectra of the homovalent analog (structure shown in Chart 2B) in blue, the band at 5600 cm^{-1} can be assigned as the $\psi \rightarrow \psi^*$ transition of the MV model. This reflects in the electronic coupling between the two Cu's ($2H_{AB}$) and derives from the

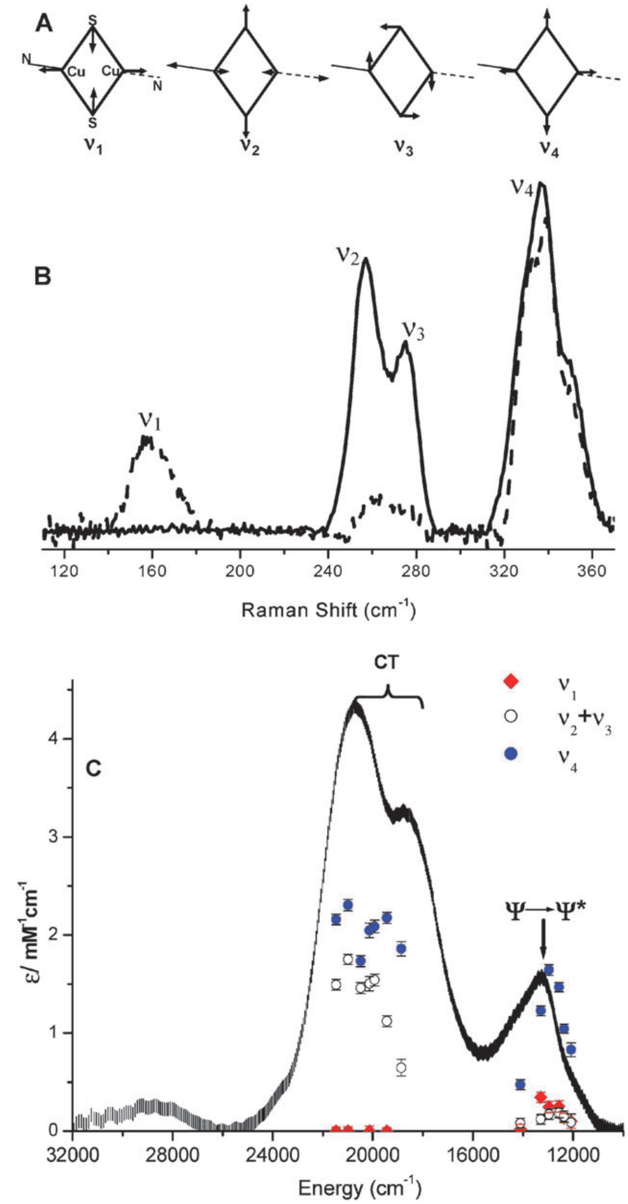

Fig. 4 (a) Raman modes of Cu$_A$ site: Cu_2S_2 core ''accordion'' bending mode (ν_1), mixed Cu–S/Cu–N stretching mode (ν_2), out-of-phase ''twisting'' Cu–S stretching mode (ν_3), breathing mode (ν_4). (b) Resonance Raman spectra of S → Cu CT band excitation (solid line), and $\psi \rightarrow \psi^*$ band excitation (dashed line); (c) Resonance Raman excitation profiles of the absorption spectrum (solid line) of Cu$_A$ site.

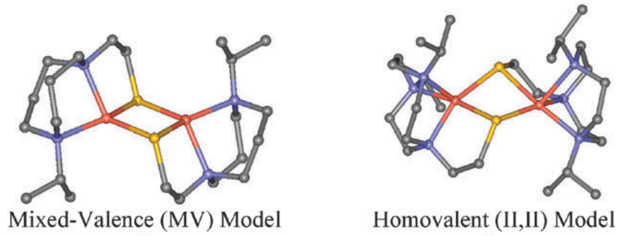

Chart 2

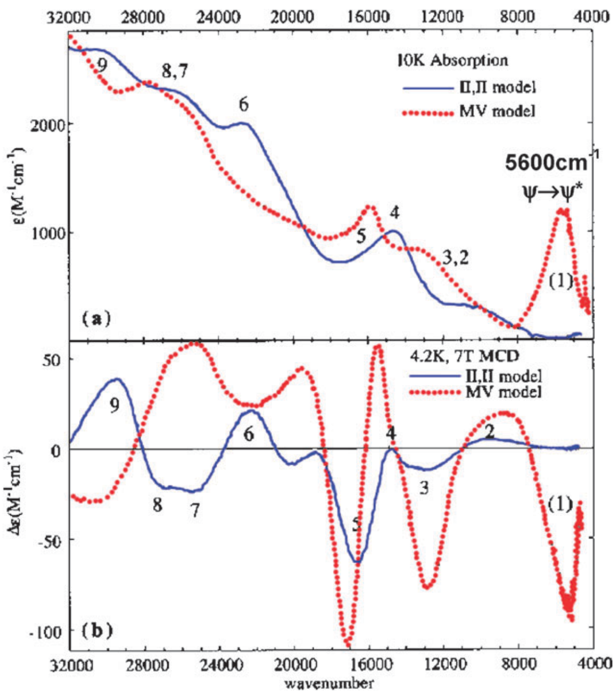

Fig. 5 Assignment of ψ–ψ* transition in the MV model complex. Comparison of low-temperature absorption (a) and MCD (b) spectra for the mixed valence model complex (red lines) and the homovalent model complex (blue lines) reveals the ψ–ψ* band at 5560 cm^{-1} that is present only in the MV complex.

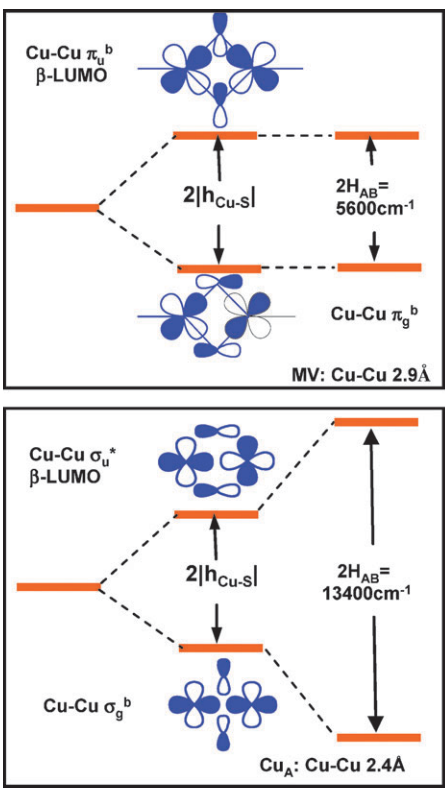

Fig. 6 D_{2h}-idealized Molecular orbital splittings in MV model and Cu_A, showing the separate contributions of Cu–S (h_{Cu-S}) and Cu–Cu (h_{Cu-Cu}) bonding interactions to $2H_{AB}$. σ and π labels refer to the symmetries of Cu–Cu interactions only.

superexchange type pathway associated with the bridging thiolates. From the schematic in Fig. 6 top that is based on density functional theory (DFT) calculations, this produces an energy splitting of the dπ orbitals on the two Cu's leading to a π_u lowest unoccupied molecular orbital (LUMO) due to its antibonding interaction with the thiolate bridges. S K-edge data in Fig. 7 bottom quantify the high sulfur covalency in this LUMO. Comparison of the MV model to Cu_A shows that the $\psi \rightarrow \psi$* transition in Cu_A shifted up in energy by 7800 cm^{-1}, yet Cu_A has somewhat less S 3p character in its LUMO (Fig. 7). This requires that there is an additional contribution to the electronic coupling between the Cu's in Cu_A ($2H_{AB}$) associated with a direct Cu–Cu bond. From the schematic based on DFT calculations in Fig. 6 bottom, this involves a strong σ-type bonding/antibonding interaction between the $d_{x^2-y^2}$ orbitals on each Cu, leading to the σ_u* RAMO of Cu_A. This gives a net large $2H_{AB}$ in Cu_A which is key to its delocalized electronic structure.

Fig. 8 includes the effect of vibronic coupling in the Q_- mode (*i.e.* eqn (2)) for Cu_A and the MV model. From Fig. 8 right, the MV model is just at the delocalized limit due to its $2H_{AB} = 5600$ cm^{-1}. Alternatively for Cu_A, the large $2H_{AB} =$ 13 400 cm^{-1} associated with the Cu–Cu bond at 2.4 Å gives a strongly stabilized, delocalized site which is critical in keeping Cu_A delocalized even in its low symmetry protein environment.

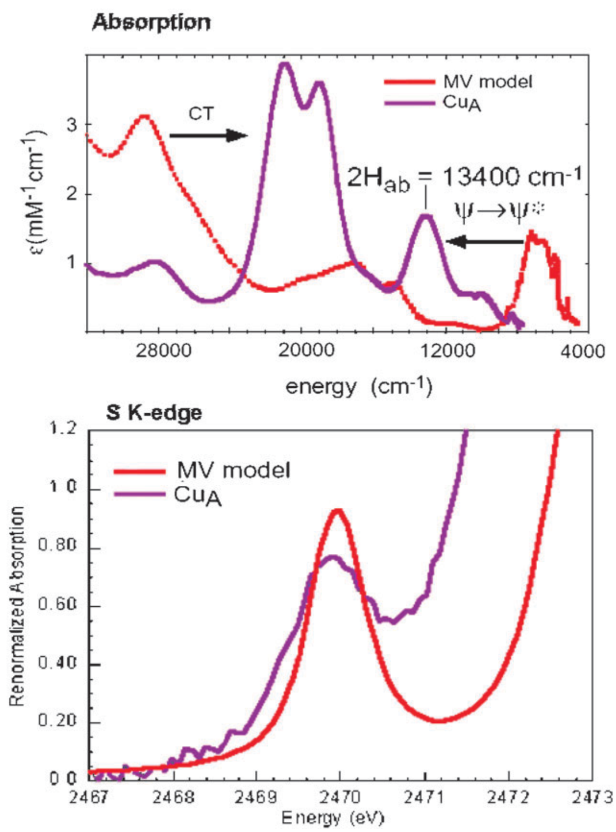

Fig. 7 The spectroscopic definition of the electronic structure of Cu_A. (a) Comparison of absorption spectra shows an increase in ψ–ψ* transition energy relative to the mixed valence model. (b) Sulfur K-edge XAS reveals similar bridging thiolate covalency in Cu_A center and the MV model.

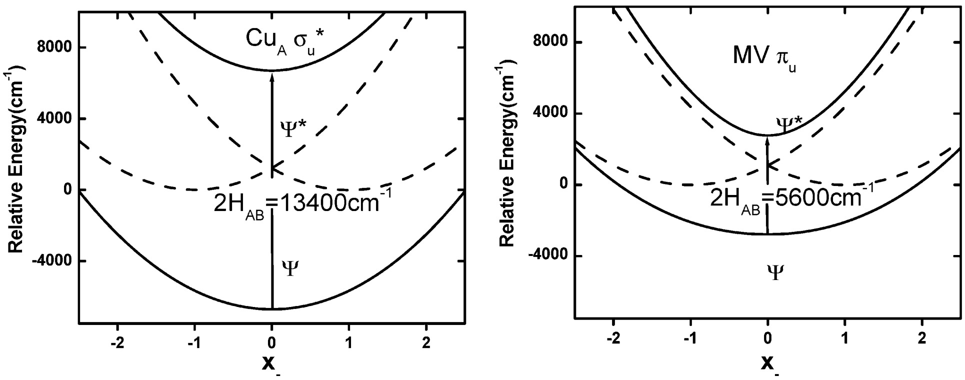

Fig. 8 Potential energy surfaces in the Q_- mode for Cu_A and the MV model showing the strong stabilization for valence delocalization in Cu_A due to metal–metal bonding.

An interesting issue has then arisen which involves the energy of the π_u state relative to the σ_u* ground state in Cu_A.[15] From Fig. 9, correlation of the low temperature MCD with the Abs spectrum of Cu_A shows two types of behavior: a derivative shaped, pseudo-A term (the derivative shape indicates an A-term description, but the temperature dependence of this signal shows that it is a combination of equal but opposite signed C-terms), in the thiolate to Cu CT region, and a negative C-term feature in the $\psi \rightarrow \psi^*$ region. MCD intensity requires two perpendicular transition moments, and in the $< D_{2h}$ symmetry of Cu_A, all the electronic transitions are unidirectional. Therefore, MCD intensity requires spin orbital (S.O.) coupling between states with perpendicular transition moments. There are two mechanisms for this: from Fig. 10 left, two excited states with perpendicular polarizations can S.O. couple in a third direction to produce equal and opposite MCD features, a pseudo-A term. This is the assignment of the MCD spectrum in the CT region of Cu_A.[22] Alternatively, there can be a low-lying (non-thermally accessible) state with a perpendicularly-polarized transition to the same excited state which can S.O. couple into the ground state in a third perpendicular direction. This is the assignment of the negative C-term of the $\psi \rightarrow \psi^*$ transition of Cu_A. The only low lying excited state capable of this coupling mechanism is π_u.[23]

TD-DFT calculations reproduce the Abs spectrum of Cu_A (Fig. 9) and give the π_u state at 3200 cm^{-1} above the σ_u* ground state. Consistent with this, the EPR spectrum of Cu_A gives an experimental $g_{||} = 2.19$. The deviation of g value from 2.0023 also derives from S.O. coupling of the π_u excited state into the σ_u ground state. The energy of the π_u can then be obtained from:

$$g_{||} \approx g_e + 8\zeta_{3d}^{Cu}\alpha^2\beta^2/\Delta_{\sigma_u^*/\pi_u}, \tag{3}$$

which (using the covalency of Cu_A described above) gives $\Delta_{\sigma_u^*/\pi_u} = 5000\ cm^{-1}$. Thus the MCD, EPR and DFT calculations all give a π_u state at $\geq 3200\ cm^{-1}$ above the σ_u* ground state for Cu_A. Alternatively, paramagnetic ^{1}H NMR studies of Cu_A from several labs show an anti-Curie behavior indicating that the π_u state was only $\sim$350 cm^{-1} above the σ_u* ground state.[24–26] The TD-DFT calculations were then used to explore the potential energy surfaces in the Cu–Cu coordinate for Cu_A. From Fig. 11, at its equilibrium geometry with Cu–Cu = 2.4–2.5 Å, the TD-DFT calculations on Cu_A give the π_u state at 3200 cm^{-1} above the ground state, and this energy splitting is consistent with the analysis of the EPR and MCD data. However, upon elongation of the Cu–Cu distance, the π_u state

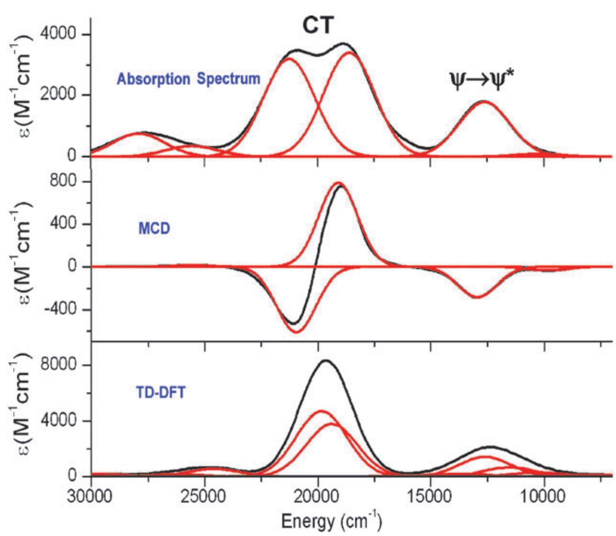

Fig. 9 (a) Room-temperature absorption, (b) low-temperature MCD spectrum of *Tt* Cu_A; (c) TD-DFT calculated absorption spectrum of the Cu_A model (total absorption – black, and individual components – red).

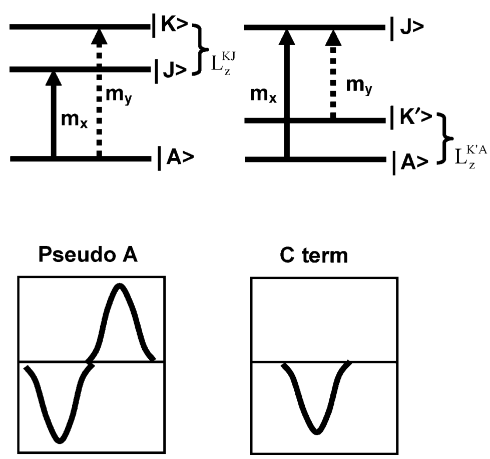

Fig. 10 MCD C-term mechanisms. m_i indicates transition intensity in i direction and L_z^{PQ} indicates spin–orbit coupling in z direction between states P and Q.

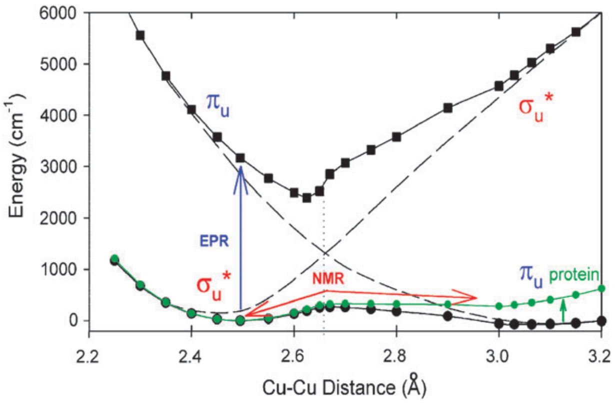

Fig. 11 The ground state and the first excited state potential energy surfaces as a function of the Cu–Cu distance (black lines refer to the Cu_A cluster in the vacuum and green – the cluster in the protein environment).

comes down in energy and the energy of the σ_u* increases. At a Cu–Cu $\sim$3 Å, the π_u is the ground state and at an energy very similar to that of the σ_u* in its equilibrium geometry of Cu–Cu = 2.4–2.5 Å.

This ground state adiabatic potential energy surface is appropriate for the thermally equilibrated states observed by ^{1}H NMR. From the Mayer bond analysis[27] in Fig. 12, the π_u state has a very similar total energy to the σ_u* state because at the long Cu–Cu distance the M–M bond is eliminated, but the net Cu–S bond strength has increased. Comparison of the green to the black surface in Fig. 11 shows a very important role of the protein. From quantum mechanics/molecular mechanics (QM/MM) calculations, the protein (through H-bond interactions with the thiolate bridges, and axial interactions) stabilizes the σ_u* ground state relative to π_u, which maintains the large electronic coupling matrix element between Cu's and keeps the state delocalized even in the low symmetry protein environment.

The issue of localization and delocalization has become important in a pH effect observed for Cu_A.[23,28] This is thought to play a role in regulating proton pumping, where the function of cytochrome *c* oxidase is to translocate protons from inside to outside the membrane to create a gradient for ATP synthesis. Upon going to low pH, the EPR spectrum of Cu_A (with 7 hyperfine lines associated with complete electron spin delocalization over 2Cu's, each with $I = 3/2$) goes to a 4-line pattern indicating hyperfine coupling to only one Cu, thus apparent localization. An equivalent spectrum is observed in a H120A mutant of Cu_A which eliminates the pH effect. Thus the low pH apparent localization (by EPR) is associated with elimination of one His ligand of Cu_A. Fig. 13 correlates the high pH EPR/Abs/MCD/EXAFS spectra to those of the low pH form and the H120A mutant. The low pH and mutant spectra are equivalent, and importantly these spectra are very similar to those of the high pH form with only a small shift in the $\psi \rightarrow \psi$* energy. In fact, excitation into this band produces the same resonance enhancement of the symmetric breathing and accordion modes in the rR spectrum indicating an equivalent excited state distortion to that observed from Cu_A at high pH (elongation of the Cu–Cu bond by

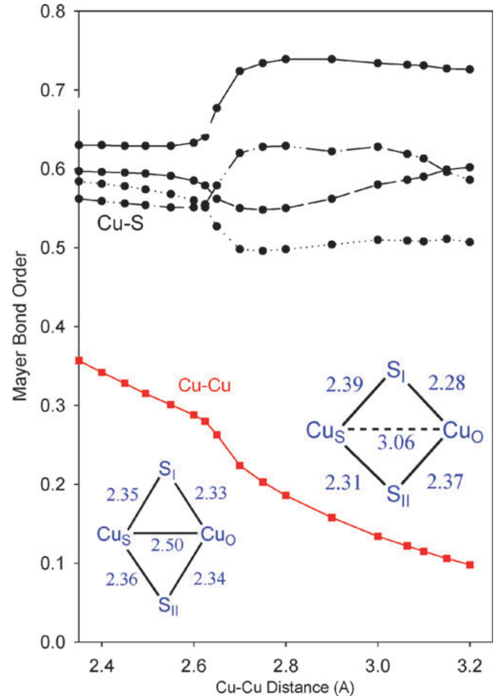

Fig. 12 Mayer bond orders for the four Cu–S bonds (black lines) and Cu–Cu bond (red line) in the ground state of Cu_A as a function of the Cu–Cu distance (the labels Cu_S and Cu_O denote the copper with a weak axial thioether sulfur and carbonyl oxygen ligand, respectively).

0.44 Å).[16] Therefore, from the excited state data, the low pH form of Cu_A is still delocalized. rR excitation into the CT region shows that upon going to low pH, one of two His vibrations at 260 cm^{-1} is eliminated, and from EXAFS, one Cu–N interaction (out of two) is lost as well. Thus in the low pH form of Cu_A where one His is protonated off, the site remains delocalized but exhibits apparent localization by EPR.

Insight into this inconsistency between EPR and Abs/rR/MCD/EXAFS was obtained from geometry optimized DFT calculations of the wild type (w.t.) Cu_A site modeling the high and low pH forms (Fig. 14). The high pH calculations give a ground state with the electron spin approximately equivalently delocalized over the two copper centers (Fig. 14A). To model the low pH site, His120 was protonated, and upon geometry optimization this ligand comes off the Cu and is replaced by a nearby H_2O molecule producing a distorted ligand field at this Cu, labeled Cu_O as it has a weak axial carbonyl oxygen ligand (Fig. 14B). Importantly, the ground state wavefunction of this perturbed structure still shows about the same delocalization over the two Cu centers. However, the distorted ligand field of Cu_O produces $\sim$1% mixing of the Cu 4s orbital into the RAMO of the binuclear site. In the high pH form, each Cu has the same relatively small negative contribution to the hyperfine coupling due to the delocalization of the electron spin over the two Cu centers. In the low pH form, the $\sim$1% 4s mixing adds a direct Fermi contact contribution to the hyperfine of Cu_O, which is large and positive. The net effect is to generate a Cu_O with very small hyperfine coupling to the electron spin, even though it

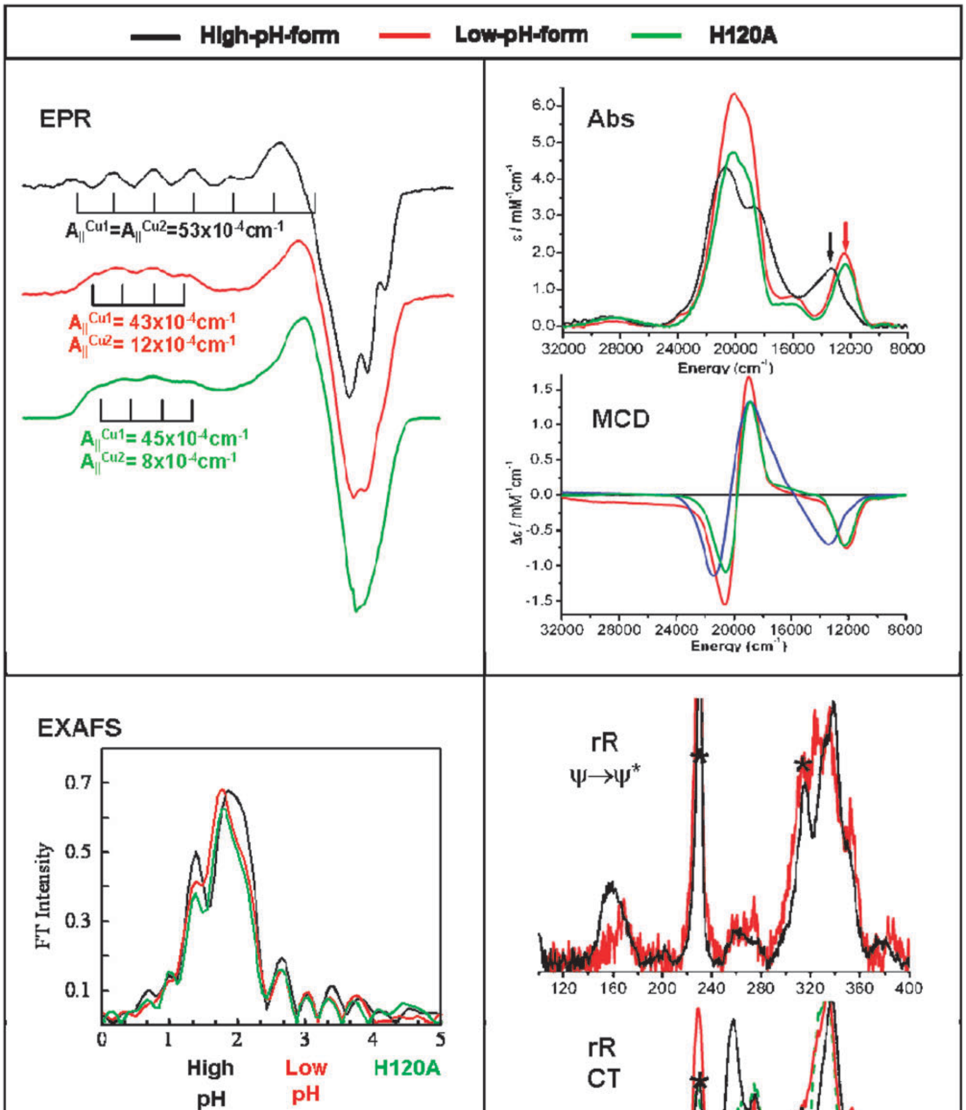

	High pH	Low pH	H120A
n Cu-N	n=1 1.92	n=0.5 1.94	n=0.5 1.93
2 Cu-S	2.27	2.26	2.27
1 Cu-Cu	2.40	2.38	2.38

Fig. 13 Comparison of the EPR/Abs/MCD/EXAFS spectra of the high pH form of Cu_A to those of the low pH form and the H120A mutant.

has about as much spin density as the non-perturbed Cu. Thus the EPR spectrum can be misleading with respect to delocalization due to the potentially large effects of small contributions to the ground state wavefunction.[23]

The delocalization in Cu_A, even with the His ligand substitution at low pH, can be understood from the potential energy surfaces in the Q_- mode of vibronic coupling in Fig. 15. The large $2H_{AB}$ keeps the sites delocalized even with up to 120 mV inequivalence[23] between the two Cu centers. Thus the strong electronic coupling between the Cu's due to their direct σ bonding interaction at 2.4 Å results in a highly delocalized center which facilitates rapid ET over long distances with low driving forces.

Localized *vs.* delocalized mixed valence 2Fe sites

We next turn to the 2Fe site in biological ET, the plant ferredoxins. Their redox couple is $Fe^{III}Fe^{III}$ to $Fe^{III}Fe^{II}$, where the reduced state is localized (from Mössbauer) and has AF coupling between the Fe's.[29] This gives an $S = 1/2$ ground state. The Fe–Fe distance is 2.73 Å and the first issue that arises is whether there is direct electronic coupling between the Fe^{III} and Fe^{II} at this distance. This was addressed through comparison of this localized $Fe^{III}Fe^{II}$ site to a complex $[Fe_2(OH)_3(tmtacn)_2]^{2+}$ (tmtacn = N,N',N''-1,4,7-trimethyltriazocyclononane) from Wieghardt and coworkers (Chart 3A)[30] which has 2Fe's held at 2.51 Å by three ^-OH bridges and is

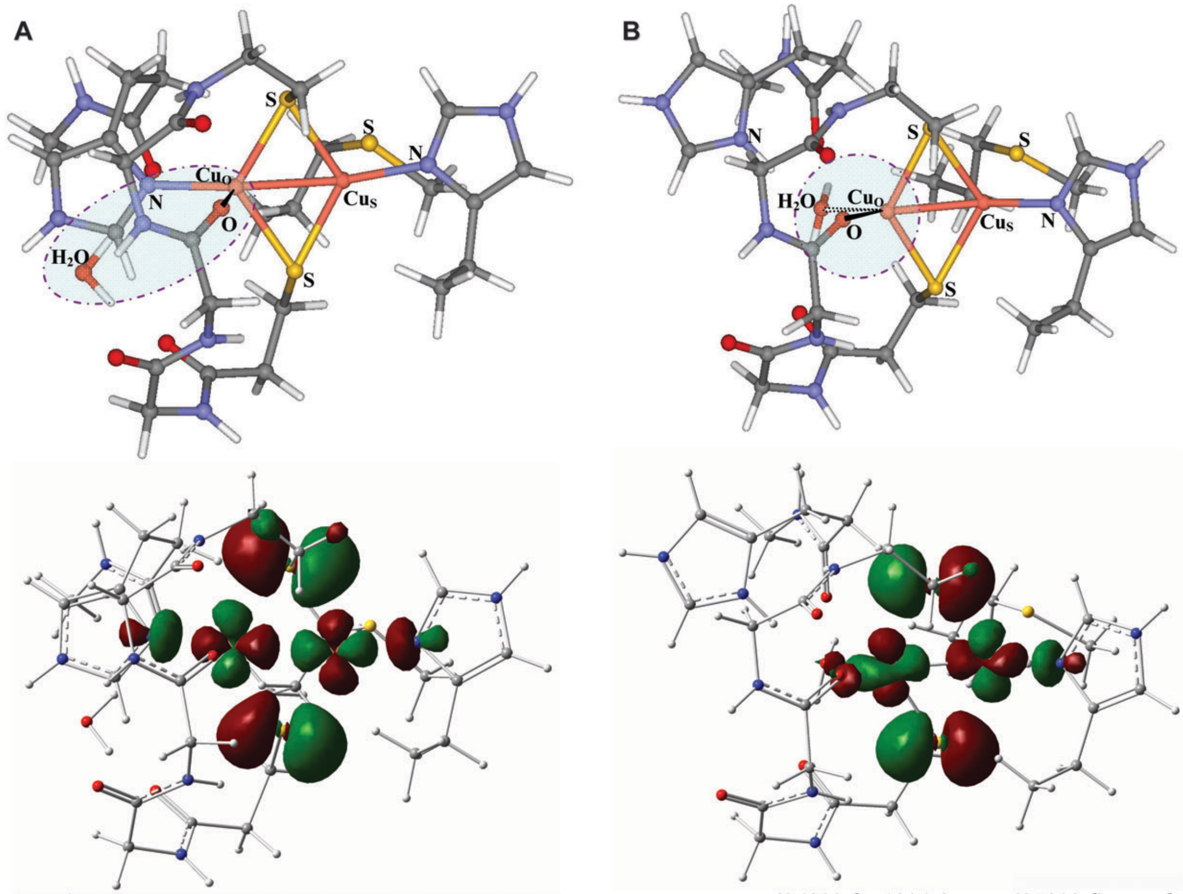

$$\psi^{w.t.}_{High\ pH} = (26\%3d)_{Cu_O} + (22\%3d)_{Cu_S} + ligand \qquad \psi_{Low\ pH} = (24\%3d + 1\%4s)_{Cu_O} + (25\%3d)_{Cu_S} + ligand$$

Fig. 14 DFT geometry optimized structures (top) and β-LUMO contours (bottom) of (a) the high pH form; (b) the low pH form/H120 mutant.

class III delocalized with a ferromagnetic $S = 9/2$ ground state.[31] Allowing for interactions between two face-sharing octahedral Fe's leads to a splitting of the ten d-orbitals due to direct Fe–Fe σ bond involving two d_{z^2} orbitals (z along Fe–Fe) and superexchange pathways through the bridging $^{-}$OH ligands. Adding 11 electrons while retaining an $S = 9/2$ ground state gives the electron configuration at the right of Fig. 16. The d_{z^2} σ-bonding/antibonding splitting is $2H_{AB}$ which for a magnetic system is $10B$ (Fig. 16), where B is the double exchange parameter.[31,32] Excitation of the extra electron in the d_{z^2} σ^b orbital into its σ* counterpart results in an electron-dipole-allowed z polarized transition which is assigned to the band at 13 500 cm^{-1} in the Abs/MCD spectra in Fig. 17.[31] This gives an experimental estimate of $10B$ for the complex. rR excitation into this transition results in enhancement of the symmetric breathing and accordion modes and generates an excited state distortion where the Fe–Fe distance increases to 2.9 Å due to this σ → σ* transition.

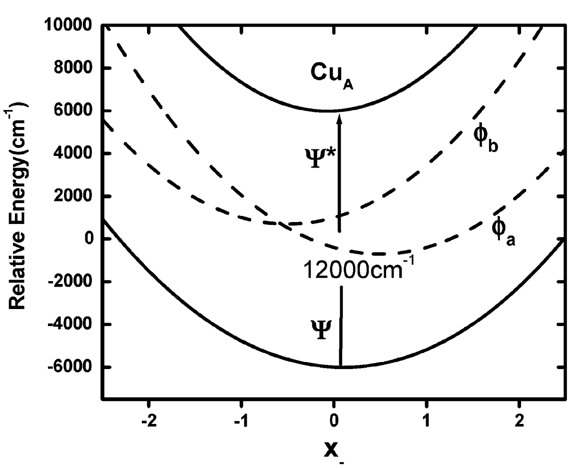

Fig. 15 Potential energy surfaces in Q_- mode for the low pH form of Cu_A showing valence delocalization due to strong metal–metal bonding.

Fitting the rR excitation profiles (Fig. 18A and 18B), the Abs band-shape, and the temperature dependence of the Abs band-shape (Fig. 18C) yields the anharmonic potential energy surfaces in the Fe–Fe coordinate in Fig. 18D.[31] From Fig. 18D the σ → σ* splitting ($10B$) in the excited state is 6800 cm^{-1}. Thus we have B in the ground (from Abs/MCD) and excited state geometries and can get an estimate of $\Delta B/\Delta r$ = 1750 cm^{-1}/Å. This allows an estimation of B for the $(Fe_2S_2)^+$ site at its 2.73 Å Fe–Fe distance of 965 cm^{-1} (this also involves a d_{z^2} σ/σ* interaction between the two-edge shared tetrahedral).[33] This is smaller than that of the complex $[Fe_2(OH)_3(tmtacn)_2]^{2+}$ (Fe–Fe distance at 2.51 Å), but still large enough to produce a large electronic coupling between the Fe's for delocalization ($2H_{AB}$ = 9650 cm^{-1}).[33]

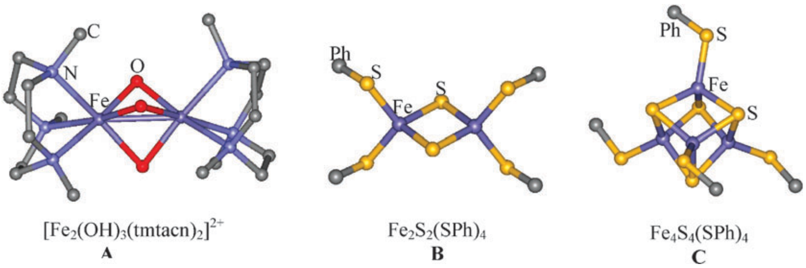

Chart 3

We next need to consider the additional interaction between the Fe's associated with their exchange coupling. The magnetic coupling of an Fe(III) $S = 5/2$ with an Fe(II) with $S = 2$ gives $S_{tot} = 1/2$, 3/2. 5/2, 7/2, 9/2 dimer states, which are split in energy by intervals of the exchange coupling, J. Delocalization of the extra electron between the two Fe's splits each spin state into g/u dimer states (Fig. 19). This splitting is described by the double exchange term in the spin Hamiltonian which is dependent on the spin state ($\Delta g/u = 2B(S + 1/2)$): the $S_{tot} = 1/2$ is split by $2B$, while the $S_{tot} = 9/2$ is split by $10B$).[31–33] This dependence of the electronic coupling on the spin state can be understood from Fig. 20, where for the ferromagnetic configuration ($S = 9/2$) the extra electron is easily delocalized between the two Fe's, while for the AF configuration ($S = 1/2$) delocalization leads to an excited state which costs energy.[34]

For the complex $[Fe_2(OH)_3(tmtacn)_2]^{2+}$, which is ferromagnetic and described by the right hand side of the B/J diagram (Fig. 19), we used SQUID magnetic susceptibility to measure the S_{tot} 9/2–7/2 splitting to get the exchange interaction between the Fe's in the tris $^{-}$OH bridged structure.[33] From the data in Fig. 21 no deviation of μ_{eff} at high temperature was observed above the error bars of the data. From fits to the data, the

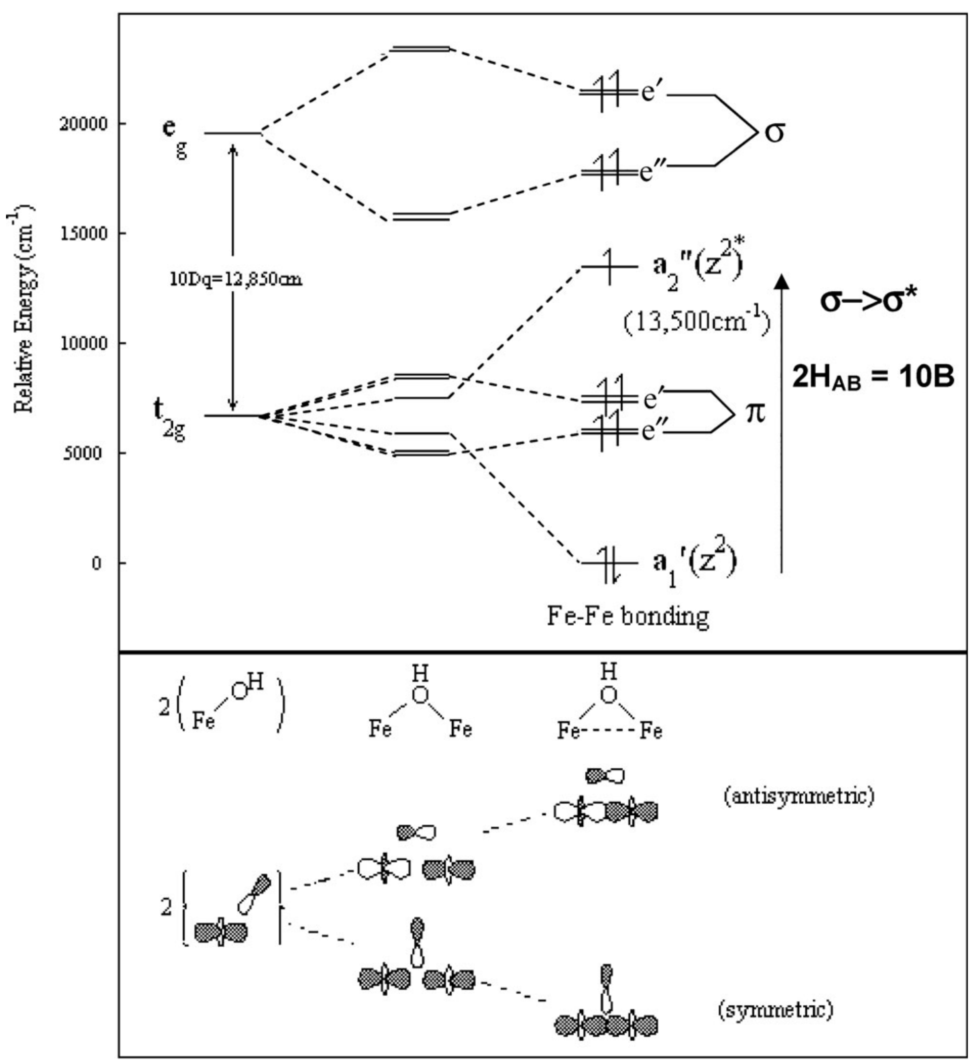

Fig. 16 Energy level diagram of the delocalized mixed valence $[Fe_2(OH)_3(tmtacn)_2]^{2+}$ complex.

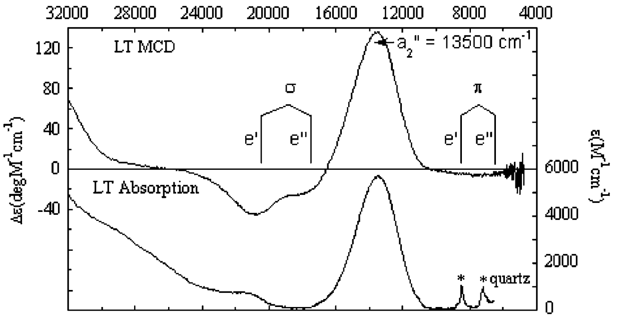

Fig. 17 MCD (top) and absorption (bottom) spectra of the mixed valent $[Fe_2(OH)_3(tmtacn)_2]^{2+}$ complex at 5 K; σ and π labels on the spectra refer to the energy level diagram of Fig. 16.

$S_{tot} = 7/2$ state must be $> 720\ cm^{-1}$ above the ground state. From Fig. 19 this splitting is given by $9J + B$, and since we know B from the Abs/MCD/rR data on this complex we can get J which must be less AF coupled than 70 cm^{-1}. We can alternatively use the MCD data in Fig. 17 which gives the splitting of the σ and π super-exchange pathways of the tris ^{-}OH bridged structure (Fig. 16) to get an excited state estimate of J (using the Hey, Thibeault, Hoffman model),[35] which is less AF coupled than 23 cm^{-1}. From these results the tris ^{-}OH bridges are not very effective in mediating AF coupling between the Fe's.[33] For the Fe_2S_2 ferredoxin site which is AF coupled with an $S = 1/2$ ground state, the left hand side of the B/J diagram in the Fig. 19 is appropriate. The S_{tot} 1/2–3/2 splitting has been measured as 315 cm^{-1}.[36] From Fig. 19 this needs to be corrected for B (S_{tot} 3/2–1/2 $= -3J–B$) which we have estimated at 965 cm^{-1} from the $\Delta B/\Delta r$ correlation in Fig. 18D.[33] This then gives a $J \sim -430$ cm^{-1} for the reduced Fe_2S_2 active site which is an order of magnitude stronger AF coupling than that of the complex $[Fe_2(OH)_3(tmtacn)_2]^{2+}$. Thus the bridging sulfide (μ_2S^{2-}) is involved in a very covalent bonding interaction with the two Fe's which results in large AF coupling.[33]

Fig. 22 combines the exchange, double exchange and vibronic coupling for these complexes. For the complex $[Fe_2(OH)_3(tmtacn)_2]^{2+}$, B is large and J is small due to the low covalency of the ^{-}OH bridges. This results in a $B/|J| > 9$ in Fig. 19 and $S_{tot} = 9/2$ ground state. This has an electronic coupling of $10B$, large enough to overcome the vibronic coupling which gives a delocalized ferromagnetic ground state as observed experimentally. For the $[Fe_2S_2]^{+}$ site, while the B is somewhat decreased, the key feature is that the AF coupling is large. This gives $B/|J| < 3$ in Fig. 19 and an $S_{tot} = 1/2$ ground state. For this spin state the electronic coupling is only $2B$, and this combines with the vibronic coupling to produce a localized $S = 1/2$ ground state (Fig. 22, right) as observed experimentally.[33]

Thus it is the large AF exchange coupling associated with the high covalency of the μ_2S^{2-} bridges that leads to localization in $[Fe_2S_2]^{+}$ sites.[33] This then raises the issue of whether going to the μ_3S^{2-} bridges in the Fe_3S_4 and Fe_4S_4 sites changes the covalency, hence the exchange coupling and its effect on delocalization.

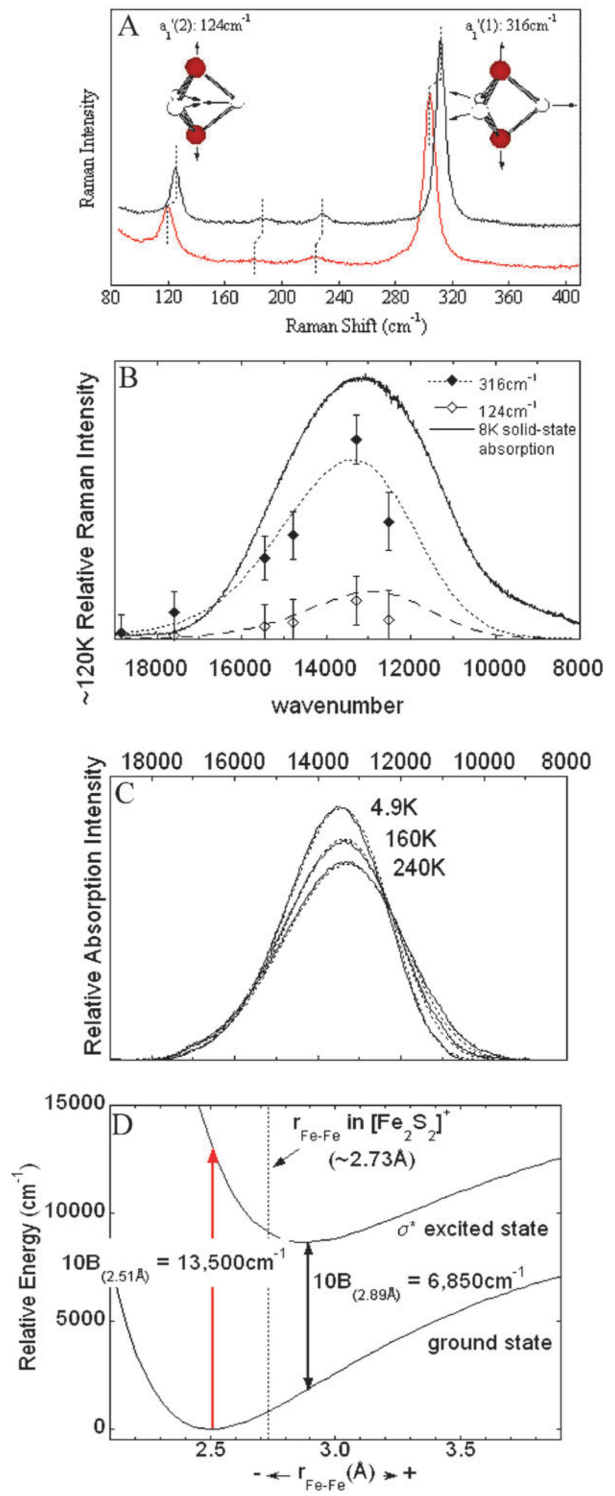

Fig. 18 (a) rRaman data of the $[Fe_2(OH)_3(tmtacn)_2]^{2+}$ complex (^{16}OH and ^{18}OH), (b) rR excitation profile obtained at 120 K, (c) Temperature dependent absorption band-shape and their corresponding fits and (d) Anharmonic potential energy surface of the $[Fe_2(OH)_3(tmtacn)_2]^{2+}$ complex along the Fe–Fe coordinate.

Fe_2S_2 (localized) *vs.* Fe_4S_4 (delocalized)

As indicated earlier, S K-edge XAS is a direct probe of covalency of Fe–S bonds. Here we use this method to evaluate the covalencies of the μ_2S^{2-} bridges in $[Fe_2S_2]^{+}$ and μ_3S^{2-} bridges in $[Fe_4S_4]^{2+}$ sites to elucidate whether this plays a role in going from the localized AF coupled $S = 1/2$ ground state in the Fe_2S_2 centers to delocalized ferromagnetically coupled

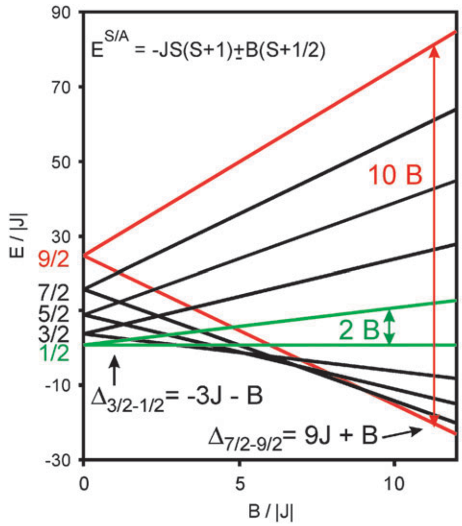

Fig. 19 Relationship of relative spin state energy and $B/|J|$.

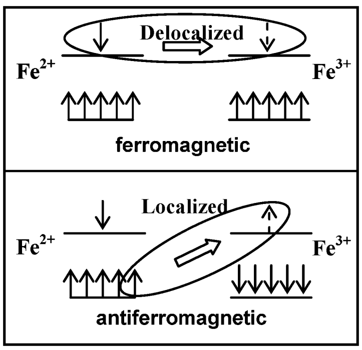

Fig. 20 Electronic configuration for ferromagnetic and antiferromagnetic coupling in a mixed valent cluster.

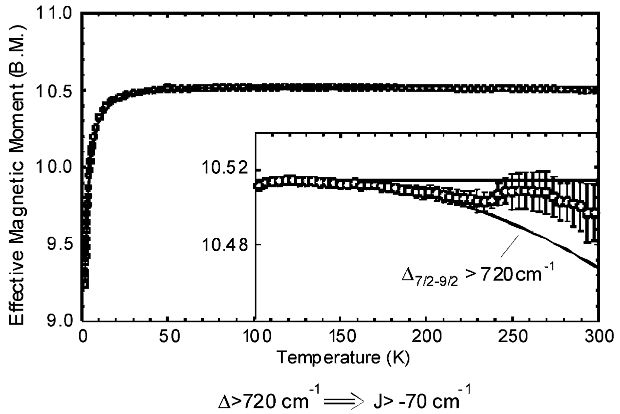

Fig. 21 Temperature dependent SQUID magnetic susceptibility of the mixed valent $[Fe_2(OH)_3(tmtacn)_2]^{2+}$ complex.

$S_{tot} = 9/2$ states in $[Fe_2S_2]^+$ sub-sites of $[Fe_4S_4]^{2+}$ clusters. The S K-edge spectrum of a 2Fe Fd model (Chart 3B) of Holm and coworkers is shown in Fig. 23A solid line.[37–39] It exhibits two peaks which can be assigned by comparison to models where the terminal thiolates are replaced by Cl^- or the bridging S^{2-} are replaced by Se^{2-}.[40] This allows assignment of the lowest peak of the pre-edge as a transition involving the μ_2S^{2-} with the higher energy feature as the thiolate 1s → 3d pre-edge transition. These sulfide and thiolate contributions to the covalency are split in energy due to differences in their Z_{eff} and the resultant shift in their 1s orbital energies.

In going to the $[Fe_4S_4]^{2+}$ cluster,[41] one broad asymmetric pre-edge peak is observed which can also be resolved by comparison to the complexes of Holm and coworkers (Chart 3C) where the thiolates are substituted with Cl^- or bridging S^{2-} with Se^{2-} (Fig. 23B).[42] This correlation shows that the μ_3S^{2-} pre-edge transition is shifted up in energy by ~1 eV relative to a μ_2S^{2-} bridge in the Fe_2S_2 cluster due to its charge donation to three Fe's.

We can now compare the covalency per Fe–S bond of the μ_3S^{2-} bridge in the $[Fe_4S_4]^{2+}$ cluster to the μ_2S^{2-} bridge in the $[Fe_2S_2]^+$ cluster, corrected to have the ions in the same $Fe^{2.5}$ redox state. From Fig. 24 the covalency of the μ_3S^{2-} of the 4Fe cluster is greatly reduced relative to the μ_2S^{2-} in the 2Fe cluster due to its covalent interaction with the third Fe.[42] It was shown in reference 42 that J scales as the covalency squared. Thus the AF exchange coupling of the μ_3S^{2-} bridges in the Fe_4S_4 cluster is reduced by more than a factor of two relative to the exchange coupling associated to the μ_2S^{2-} bridges in the Fe_2S_2 cluster. As shown in Fig. 25 this, combined with a larger B (DFT calculated) due to the shorter Fe–Fe distance in the Fe_4S_4 cluster, leads to a $B/|J| > 9$ and an $S_{tot} = 9/2$ ground state. The large electronic coupling in the $S_{tot} = 9/2$ state ($10B$) now overcomes vibronic coupling[42] and leads to the delocalization observed experimentally.[29]

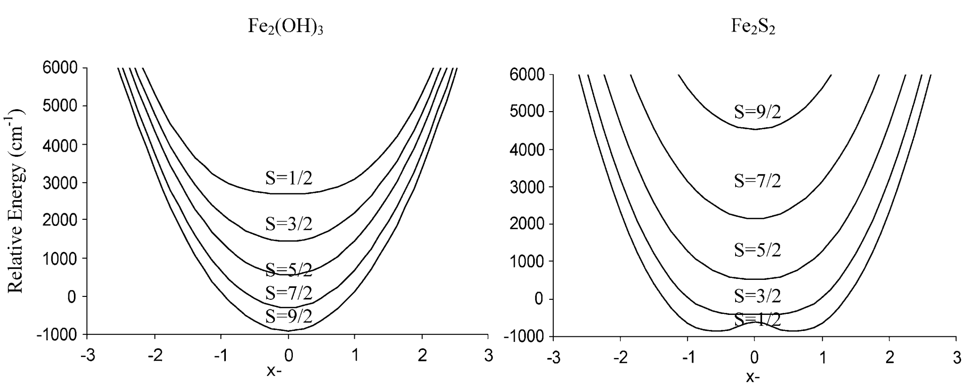

Fig. 22 Potential energy surface of different spin states for the mixed valent $[Fe_2(OH)_3(tmtacn)_2]^{2+}$ (left) and the $[Fe_2S_2]^+$ (right) clusters.

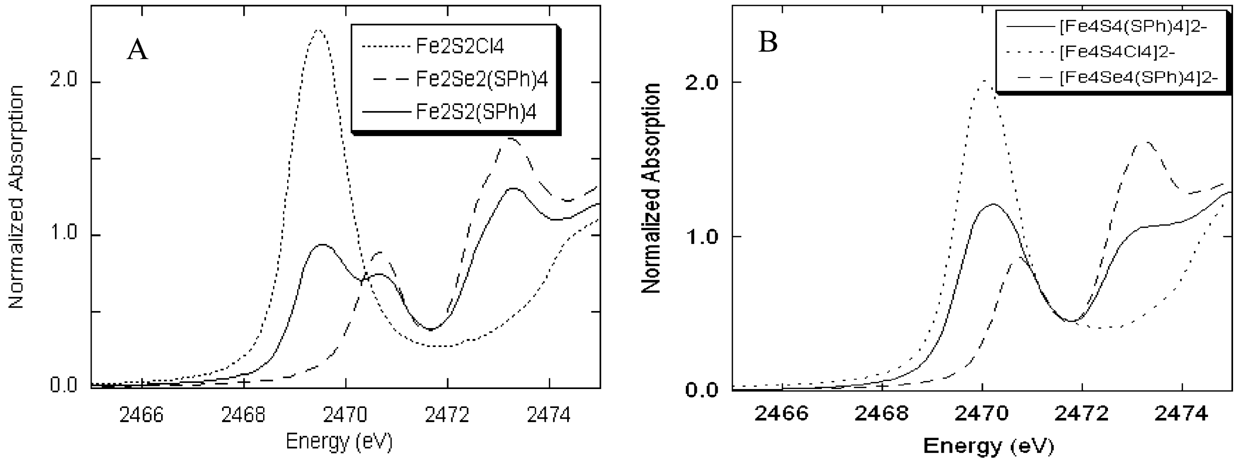

Fig. 23 S K-edge XAS of (a) $Fe_2S_2(SPh)_4$ (—), $Fe_2Se_2(SPh)_4$ (—) and $Fe_2S_2Cl_4$ (...) and (b) $Fe_4S_4(SPh)_4$ (—), $Fe_4Se_4(SPh)_4$ (—) and $Fe_4S_4Cl_4$ (...).

In summary, the polynuclear ET sites in biology have significant M–M σ bonding interactions. In Cu_A this leads to delocalization even in the low symmetry protein environment. In the 2Fe Fds this is opposed by a large AF exchange coupling associated with the highly covalent μ_2S^{2-} bridges. The latter is greatly decreased upon sulfide bridging to additional Fe centers in the higher nuclearity iron–sulfur clusters (*i.e.* μ_3S^{2-}) leading to their delocalization and associated redox properties.

Having developed an understanding of covalency and its effects on the electronic structure of the iron–sulfur clusters using S K-edge spectroscopy, we can now use this method to evaluate the effects of the protein on the cluster to control reactivity.

Functional significance

An important problem in bioinorganic chemistry has been to understand why structurally congruent $[Fe_4S_4]^{2+}$ clusters in the HiPIP's are oxidized while in Fds these are reduced.[43] From our S K-edge data in Fig. 26, the edges, and hence covalencies of HiPIPs are very similar to that of the models of

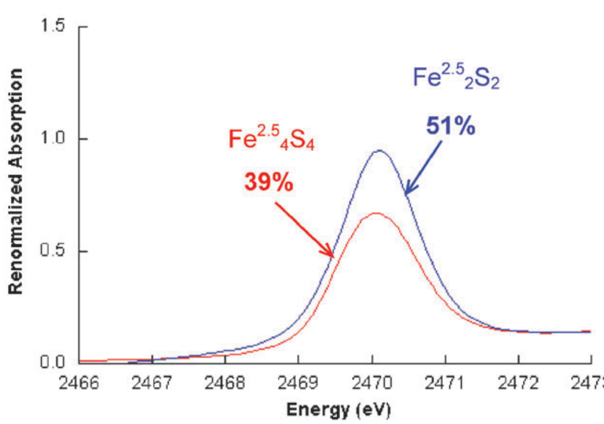

Fig. 24 Predicted bridging sulfide covalency of a hypothetical delocalized $[Fe_2S_2]^+$ cluster.

Holm and coworkers with alkyl thiolate terminal ligands (Fig. 26, blue).[44] Alternatively, the 4Fe Fds have significantly decreased S K-edge intensity, and hence Fe–S covalency (Fig. 26, red).[45] This decrease in covalency reflects the local H-bonding from the protein environment to the $[Fe_4S_4]^{2+}$cluster that tunes its reduction potential. The origin of this decrease in intensity was elucidated by S K-edges on the perturbed protein active sites in Fig. 27.[46] The 4Fe cluster in Fd is exposed to solvent on the surface of the protein. Upon lyophilizing Fd, the S K-edge intensity reversibly increases (Fig. 27, red solid to dashed). Alternatively, in HiPIP the cluster is buried in the protein. If we reversibly unfold HiPIP to expose the cluster to solvent the intensity significantly decreases (Fig. 27, blue solid to dashed). *Thus it is H-bonding of water to the exposed cluster in Fds that decreases the covalency of the* Fe_4S_4 *clusters.*

The reduction potential of Fd is ~800 mV above that of the model complex of Holm and coworkers.[47] From a correlation of covalency with E° in Fig. 28,[46] this decrease in *S* covalency due to the local H-bonds corresponds to ~450 mV of the increase in potential in Fd. The non-local environment electrostatics contributes about an additional 350 mV to the increase in potential. This raises the intriguing possibility that E° can be regulated by protein–protein and protein–DNA interactions which effect cluster solvation.[46]

The buried nature of the HiPIP Fe_4S_4 active site raises the question of how it can participate in rapid ET with its redox partner at the surface.[43] From Fig. 29A oxidation of HiPIP leads to a large increase of S K-edge intensity, much more than expected in going from 18 to 19 valence holes on the Fe_4S_4 cluster.[44] This indicates that the RAMO has a great deal of S character which is consistent with DFT calculations (Fig. 29A inset). This high ligand character can strongly couple the RAMO of the Fe_4S_4 cluster into super-exchange pathways for ET to redox partners on the surface.[44]

A large decrease in Fe–S covalency is observed upon reducing a $[Fe_4S_4]^{2+}$ model complex to the $[Fe_4S_4]^+$ state (Fig. 29B).[44] However DFT calculations show that the RAMO involved in the Fd couple (Fig. 29B inset) is

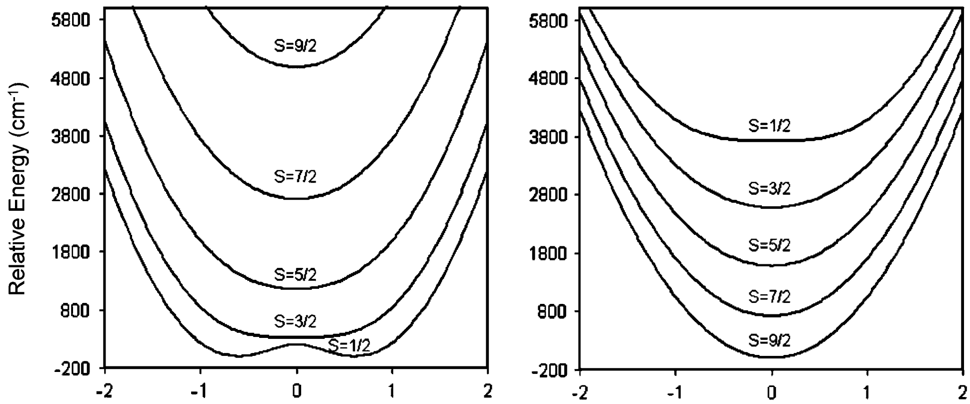

Fig. 25 Potential energy surface of different spin states for the mixed valent $Fe_2S_2^+$ sub-unit in Fe_2S_2 (left) and Fe_4S_4 (right) clusters.

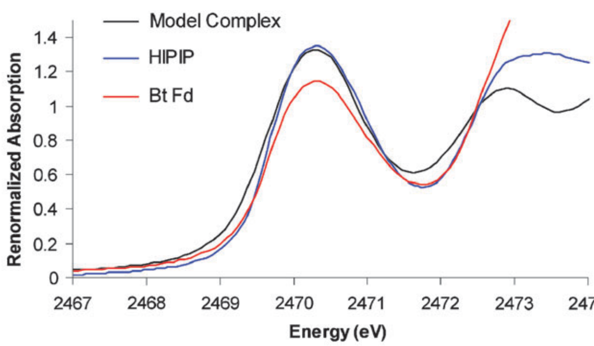

Fig. 26 S K-edge of a Fe_4S_4 Alkyl thiolate model complex (—), HiPIP (—) and Fd (—) in the resting state of the cluster.

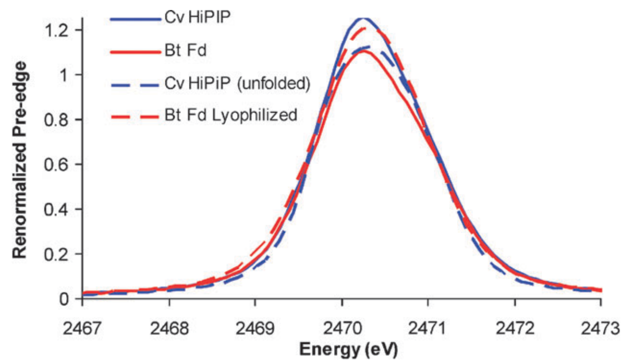

Fig. 27 Background subtracted S K-edge XAS of resting HiPIP (blue) *vs.* unfolded HiPIP (dashed blue) and resting Fd (red) *vs.* lyophilized Fd (dashed red).

primarily metal based (>90% Fe 3d in the wave-function) and thus the total Fe–S covalency should not be affected in a reduction process involving this RAMO. This implies that redox in Fd proteins involves large electronic relaxation which can facilitate ET by lowering the reorganization energy of the process.

Finally there is an additional interesting role of coupling the $[Fe_2S_2]^+$ delocalized $S = 9/2$ subsite into the higher nuclearity clusters. Oxidation of this subsite would lead to an $S_{tot} = 5$ spin state which is 0.9 eV above the AF $S_{tot} = 0$ ground state of the oxidized homo-dimer. Alternatively, using the $[Fe_3S_4]^0$

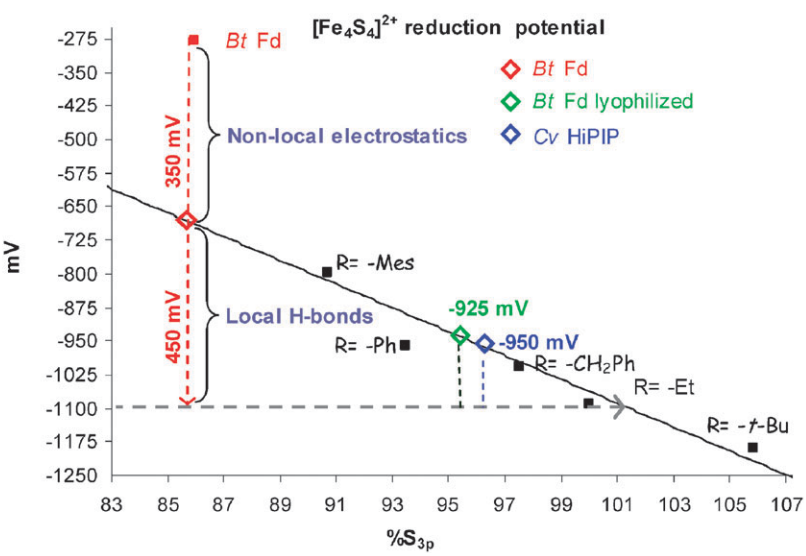

Fig. 28 Plot of total Fe–S covalency as a function of $[Fe_4S_4]^{2+}$ reduction potential *vs.* NHE for a series of $[Fe_4S_4(SR)_4]$ complexes (filled black) and *Bt* Fd (filled red). The empty squares represent the predicted (using covalency) $[Fe_4S_4]^{2+}$ electrochemical potentials. The $[Fe_4S_4]^{2+}$ reduction potential for the reference complex $[Fe_4S_4(SEt)_4]^{2-}$ is indicated by the horizontal dashed grey line.

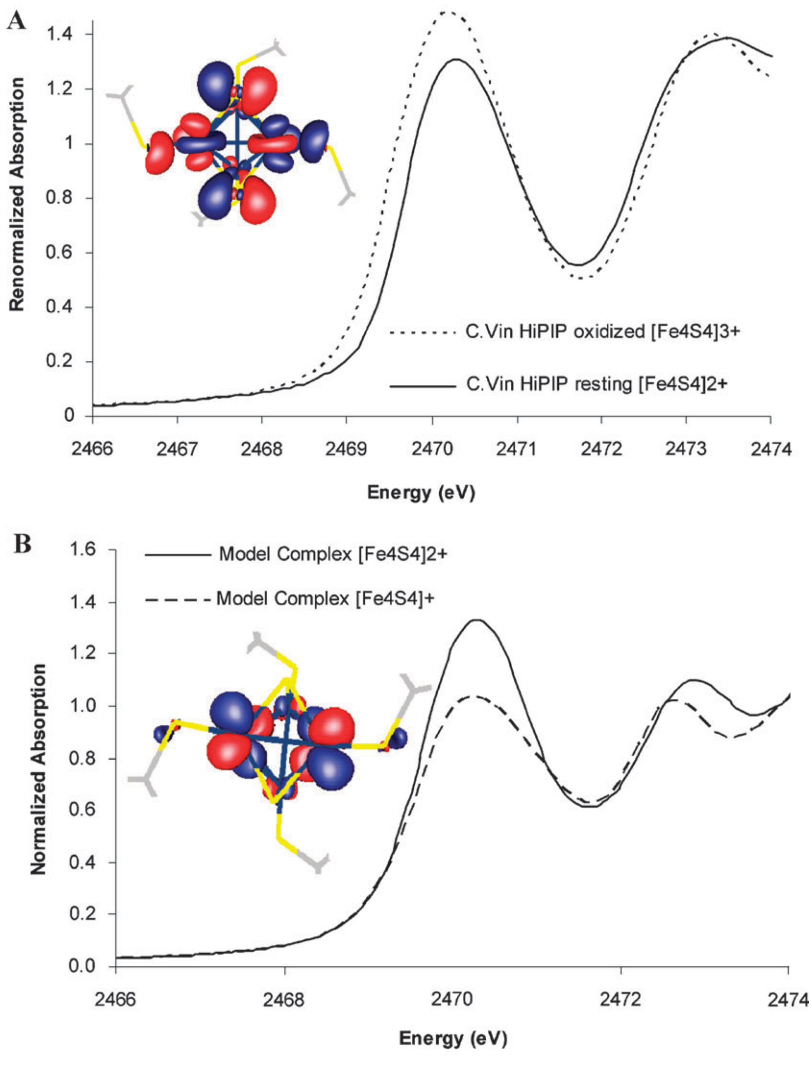

Fig. 29 (a) S K-edge XAS of HiPiP protein in its resting $[Fe_4S_4]^{2+}$ form (—), and in its oxidized (—) form, (inset) RAMO for HiPIP (b) S K-edge XAS of a synthetic model complex in the $[Fe_4S_4]^{2+}$ form (—) and in its reduced (— — —) form, (inset) RAMO for Fd.

cluster as a model, the $[Fe_2S_2]^+$ $S = 9/2$ subsite is AF coupled to the third Fe^{III} to give an $S_{tot} = 2$ ground state. Oxidation of the $[Fe_3S_4]^0$ cluster gives an $S_{tot} = 3/2$ state which is only 0.1 eV above its $S_{tot} = 1/2$ ground state (Fig. 30).[48] Thus the spin topology of the $[Fe_3S_4]^0$ and the higher nuclearity clusters can lower the spin barrier for ET.

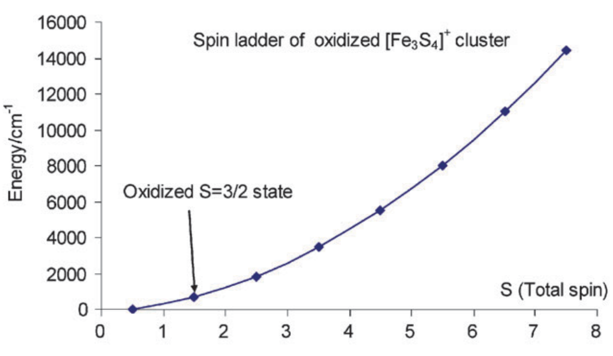

Fig. 30 Calculated spin ladder for a $[Fe_3S_4]^{1+}$ cluster (High Spin $S = 15/2$ to Low Spin $S = 1/2$). Oxidation of reduced $[Fe_3S_4]^0$ cluster gives $S = 3/2$ state.

Summary

In earlier reviews we have focused on the blue copper sites as the ''H-atom'' of bioinorganic chemistry and considered how its electronic structure is tuned for rapid ET.[8] Here we have extended these considerations to multi-nuclear ET sites where direct σ bonding interactions can lead to electron delocalization between metal ions and enhance redox properties by tuning E°, lowering λ and increasing electronic coupling into super-exchange pathways through the protein. In Cu_A the high covalency of the thiolate bridging ligands further increases the electronic coupling between the Cu and enhances delocalization. Alternatively, for the iron sulfur dimers with more than one unpaired electron on each metal ion, the very covalent μ_2-bridging sulfides provide efficient superexchange pathways for exchange coupling the additional electron spins which oppose delocalization and lead to a localized, antiferromagnetically coupled ground state in the reduced Fe_2S_2

proteins. In going to the Fe_3S_4 and Fe_4S_4 clusters, their μ_3S^{2-} bridges are less covalent/Fe–S bond and this allows electron delocalization in these higher nuclearity clusters. The covalency of these clusters can be strongly affected by the protein environment, which can control redox properties (Fe_4S_4 oxidation in HiPIP and reduction in ferredoxin) and provide effective electronic coupling through the protein for long range ET.

Acknowledgements

This research was supported by the NSF Grant CHE 0446304 (E.I.S). Past and present graduate students and postdocs, who have contributed this science, are greatly acknowledged. We also thank our collaborators who have made beautiful biological and inorganic molecules available for our studies.

References

1 R. H. Holm, P. Kennepohl and E. I. Solomon, *Chem. Rev.*, 1996, **96**, 2239.
2 J. M. Nocek, J. S. Zhou, S. De Forest, S. Priyadarshy, D. N. Beratan, J. N. Onuchic and B. M. Hoffman, *Chem. Rev.*, 1996, **96**, 2459.
3 P. J. Stephens, D. R. Jollie and A. Warshel, *Chem. Rev.*, 1996, **96**, 2491.
4 T. Tsukihara, H. Aoyama, E. Yamashita, T. Tomizaki, H. Yamaguchi, K. Shinzawa-Itoh, R. Nakashima, R. Yaono and S. Yoshikawa, *Science*, 1995, **269**, 1069.
5 S. Iwata, C. Ostermeier, B. Ludig and H. Michel, *Nature*, 1995, **376**, 660.
6 R. A. Marcus and N. Sutin, *Biochim. Biophys. Acta*, 1985, **811**, 265.
7 M. D. Newton, *Chem. Rev.*, 1991, **91**, 767.
8 E. I. Solomon, R. K. Szilagyi, S. D. George and L. Basumallick, *Chem. Rev.*, 2004, **104**, 419.
9 E. I. Solomon, *Inorg. Chem.*, 2006, **45**, 8012.
10 E. Solomon and M. Hanson, in *Inorganic Electronic Structure and Spectroscopy*, eds. E. I. Solomon and A. P. B. Lever, Wiley, New York, 1999, vol. II.
11 M. B. Robin and P. Day, *Adv. Inorg. Chem. Radiochem.*, 1967, **10**, 247.
12 P. Kroneck, W. Antholine, J. Riester and W. Zumft, *FEBS Lett.*, 1988, **242**, 70.
13 S. B. Piepho, E. R. Krausz and P. N. Schatz, *J. Am. Chem. Soc.*, 1978, **100**, 2996.
14 S. D. George, M. Metz, R. K. Szilagyi, H. Wang, S. P. Cramer, Y. Lu, W. B. Tolman, B. Hedman, K. O. Hodgson and E. I. Solomon, *J. Am. Chem. Soc.*, 2001, **123**, 5757.
15 S. I. Gorelsky, X. Xie, Y. Chen, J. A. Fee and E. I. Solomon, *J. Am. Chem. Soc.*, 2006, **128**, 16452.
16 D. R. Gamelin, D. W. Randall, M. T. Hay, R. P. Houser, T. C. Mulder, G. W. Canters, S. d. Vries, W. B. Tolman, Y. Lu and E. I. Solomon, *J. Am. Chem. Soc.*, 1998, **120**, 5246.
17 S. E. Wallace-Williams, C. A. James, S. de Vries, M. Saraste, P. Lappalainen, J. van der Oost, M. Fabian, G. Palmer and W. H. Woodruff, *J. Am. Chem. Soc.*, 1996, **118**, 3986.
18 C. R. Andrew, R. Fraczkiewicz, R. S. Czernuszewicz, P. Lappalainen, M. Saraste and J. Sanders-Loehr, *J. Am. Chem. Soc.*, 1996, **118**, 10436.
19 S.-Y. Lee and E. J. Heller, *J. Chem. Phys.*, 1979, **71**, 4777.
20 R. P. Houser, V. G. Young, Jr and W. B. Tolman, *J. Am. Chem. Soc.*, 1996, **118**, 2101.
21 K. Williams, D. Gamelin, L. B. LaCroix, R. P. Houser, W. B. Tolman, T. C. Mulder, S. de Vries, B. Hedman, K. O. Hodgson and E. I. Solomon, *J. Am. Chem. Soc.*, 1997, **119**, 613.
22 F. Neese and E. I. Solomon, *Inorg. Chem.*, 1999, **38**, 1847.
23 X. Xie, S. I. Gorelsky, R. Sarangi, D. K. Garner, H. J. Hwang, K. O. Hodgson, B. Hedman, Y. Lu and E. I. Solomon, *J. Am. Chem. Soc.*, in press.
24 J. Salgado, G. Warmerdam, L. Bubacco and G. W. Canters, *Biochemistry*, 1998, **37**, 7378.
25 R. Holz, M. Alvarez, W. Zumft and D. Dooley, *Biochemistry*, 1999, **38**, 11164.
26 I. Bertini, K. Bren, A. Clemente, J. Fee, H. Gray, C. Luchinat, B. Malmstrom, J. Richards, D. Sanders and C. Slutter, *J. Am. Chem. Soc.*, 1996, **118**, 11658.
27 I. Mayer, *Chem. Phys. Lett.*, 1983, **97**, 270.
28 H. J. Hwang and L. Lu, *Proc. Natl. Acad. Sci. U. S. A.*, 2004, **101**, 12842.
29 H. Beinert, R. H. Holm and E. Münck, *Science*, 1997, **277**, 653.
30 S. Drueke, P. Chaudhuri, K. Pohl, K. Wieghardt, X. Q. Ding, E. Bill, A. Sawaryn, A. X. Trautwein, H. WIinkler and S. J. Gurman, *J. Chem. Soc., Chem. Commun.*, 1989, **1**, 59.
31 D. R. Gamelin, E. L. Bominaar, C. Mathoniere, M. L. Kirk, K. Wieghardt, J. J. Girerd and E. I. Solomon, *Inorg. Chem.*, 1996, **35**, 4323.
32 G. Blondin and J.-J. Girerd, *Chem. Rev.*, 1990, **90**, 1359.
33 D. R. Gamelin, E. L. Bominaar, M. L. Kirk, K. Wieghardt and E. I. Solomon, *J. Am. Chem. Soc.*, 1996, **118**, 8085.
34 L. Noodleman and E. J. Baerends, *J. Am. Chem. Soc.*, 1984, **106**, 2316.
35 P. J. Hay, J. C. Thibeault and R. Hoffmann, *J. Am. Chem. Soc.*, 1975, **97**, 4884.
36 L. Petersson, R. Cammack and K. K. Rao, *Biochim. Biophys. Acta*, 1980, **622**, 18.
37 J. J. Mayerle, R. B. Frankel, R. H. Holm, J. A. Ibers, W. D. Phillips and J. F. Weiher, *Proc. Natl. Acad. Sci. U. S. A.*, 1975, **70**, 2429.
38 P. V. Rao and R. H. Holm, *Chem. Rev.*, 2004, **104**, 527.
39 K. Rose, S. E. Shadle, T. Glaser, S. de Vries, A. Cherepanov, G. W. Canters, B. Hedman, K. O. Hodgson and E. I. Solomon, *J. Am. Chem. Soc.*, 1999, **121**, 2353.
40 J. G. Reynolds and R. H. Holm, *Inorg. Chem.*, 1981, **20**, 1873.
41 B. A. Averill, T. Herskovitz, R. H. Holm and J. A. Ibers, *J. Am. Chem. Soc.*, 1973, **95**, 3523.
42 T. Glaser, K. Rose, S. E. Shadle, B. Hedman, K. O. Hodgson and E. I. Solomon, *J. Am. Chem. Soc.*, 2001, **123**, 442.
43 C. W. J. Carter, J. F. Kraut, S. T., R. A. Alden, L. C. Sieker, E. T. Adman and L. H. Jensen, *Proc. Natl. Acad. Sci. U. S. A.*, 1972, **69**, 3526.
44 A. Dey, T. Glaser, M. M. Couture, L. D. Eltis, R. H. Holm, B. Hedman, K. O. Hodgson and E. I. Solomon, *J. Am. Chem. Soc.*, 2004, **126**, 8320.
45 T. Glaser, I. Bertini, J.-J. G. Moura, B. Hedman, K. O. Hodgson and E. I. Solomon, *J. Am. Chem. Soc.*, 2001, **123**, 4859.
46 A. Dey, J. F. E. Dey, Jr, M. W. W. Adams, E. Babini, Y. Takahashi, K. Fukuyama, K. O. Hodgson, B. Hedman and E. I. Solomon, *Science*, 2007, **318**, 1464.
47 B. V. DePamphilis, B. A. Averill, T. Herskovitz, L. Que, Jr and R. H. Holm, *J. Am. Chem. Soc.*, 1974, **96**, 4159.
48 A. Dey, T. Glaser, J.-J. G. Moura, R. H. Holm, B. Hedman, K. O. Hodgson and E. I. Solomon, *J. Am. Chem. Soc.*, 2004, **126**, 16868.